



Cite this: *Nanoscale Adv.*, 2024, 6, 6123Received 14th June 2024
Accepted 21st October 2024

DOI: 10.1039/d4na00497c

rsc.li/nanoscale-advances

Green synthesis of porphyrin-based self-assembled nanocubes for augmented sono-photodynamic inactivation of bacteria: a sustainable approach towards advanced antimicrobial strategies†

Pradeep Singh Thakur ^a and Muniappan Sankar ^{*ab}

Recent focus on sustainable nanoparticle synthesis highlights bio-inspired nano-antimicrobials advantages over chemically synthesized counterparts. This study pioneers the green synthesis of porphyrinic nanocubes, demonstrating potent antibacterial activity through sono-photodynamic inactivation. This sustainable approach holds promise in combating antibiotic resistance.

Pathogenic bacterial infections are serious life-threatening conditions worldwide due to their high morbidity and mortality.¹ Taking coronavirus disease 2019 (COVID-19) as an example, many individuals have succumbed to secondary bacterial infections rather than the virus itself.² Currently, antibiotic treatment is the primary strategy for combating bacterial infections. However, the extensive misuse of antibiotics has led to the widespread emergence of bacterial resistance, even resulting in the creation of superbugs.³ In some instances, antibiotic resistance poses a far greater threat to public health than COVID-19.⁴ Skin and soft tissue infections, among the most common types of infections, are particularly concerning as they are associated with both Gram-positive and Gram-negative bacteria. For example, *Staphylococcus aureus* (*S. aureus*) often initiates infections, while *Escherichia coli* (*E. coli*) becomes predominant in later stages, continuously threatening public health.^{5–7} This scenario underscores the urgent need for alternative treatments that are not only effective but also environmentally benign and biocompatible.

In this pursuit, the convergence of green chemistry principles and nanotechnology has paved the way for sustainable and effective antimicrobial solutions.^{8,9} Green synthesis, characterized by its reliance on natural extracts and environmentally

benign procedures, has emerged as a pivotal avenue for nanoparticle production. Leveraging biological resources such as plant extracts for the synthesis of nanoparticles offers a cost-effective and scalable method, while simultaneously reducing the environmental impact associated with conventional chemical synthesis.^{10–12} Green tea extract (GTE), rich in polyphenols and antioxidants, plays a crucial role in this process, acting as both a reducing and stabilizing agent, which not only enhances the biocompatibility of the nanoparticles but also contributes to their therapeutic efficacy, making it an ideal candidate for eco-friendly nanomaterial synthesis.^{13–15}

Sono-photodynamic therapy (SPDT) combines sonodynamic and photodynamic modalities to enhance antibacterial efficacy.^{16–20} Ultrasound waves improve nanoparticle penetration into bacterial cells, while subsequent light activation triggers reactive oxygen species, leading to bacterial inactivation. This combined approach offers a more effective and targeted antibacterial strategy compared to conventional therapies. Unlike photodynamic therapy (PDT), limited by light penetration, sonodynamic therapy (SDT) utilizes deeper-penetrating ultrasound waves, extending the therapeutic reach.^{21,22}

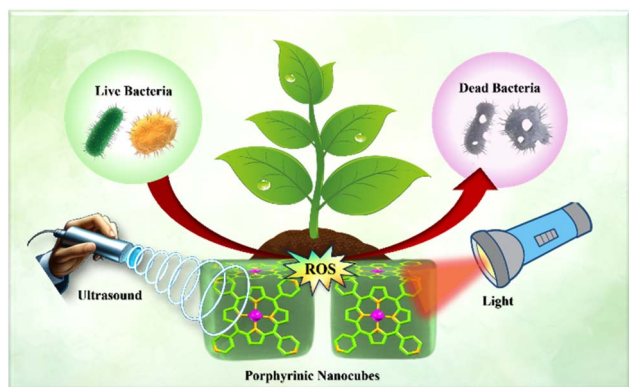
Among various nanomaterials, porphyrin-based nanoparticles stand out due to their unique photophysical properties, making them ideal candidates for antimicrobial SPDT applications. These versatile molecules can be activated by both light and ultrasound (US) to produce reactive oxygen species (ROS).^{23,24} Porphyrins also offer precise synthetic modifications, excellent biodegradability, and low cytotoxicity when not activated, making them well-suited for targeted therapies and diagnostics in biomedical applications.^{25,26}

This research focuses on the biogenic green synthesis of zinc *meso*-tetrakis(4-pyridyl)porphyrin (ZnTPyP) self-assembled nanocubes using green tea extract (GTE), aiming to harness the dual capabilities of sonodynamic and photodynamic therapies for bacterial inactivation. To the best of our knowledge, this study represents the first instance of employing plant extract (composition analysis by HPLC (Table S1†) and IR spectroscopy (Table S2†)) for the green synthesis of porphyrin-

^aCentre for Nanotechnology, Indian Institute of Technology Roorkee, Roorkee 247667, India. E-mail: m.sankar@cy.iitr.ac.in

^bDepartment of Chemistry, Indian Institute of Technology Roorkee, Roorkee 247667, India

† Electronic supplementary information (ESI) available: Materials, characterization, details on experimental procedures, and supplementary data figure. See DOI: <https://doi.org/10.1039/d4na00497c>



Scheme 1 Schematic representation of the bioinspired porphyrin-based nano-sono-photosensitizers. The porphyrin-based self-assembled nanocubes were synthesized via bioinspired route and utilized for the sono-photodynamic inactivation of bacteria.

based nanoparticles. The resultant ZnTPyP nanocubes exhibited outstanding bactericidal efficiency, achieving 99.995% against *S. aureus* and 99.92% against *E. coli* under combined ultrasound (1.0 MHz, 1.5 W cm²) and 670 nm deep-red light irradiation within 20 minutes (Scheme 1).

The biogenic or green synthesis of porphyrinic nanocubes (GS-ZnTPyP-NCs) was optimized using Dynamic Light Scattering (DLS) analysis and Field-Emission Scanning Electron Microscopy (FESEM) imaging. Table S3, ESI† represents successive DLS measurements taken every 6 hours during the self-assembly of porphyrinic nanocubes, to monitor key parameters such as hydrodynamic size, poly-dispersity index (PDI), and zeta potential over time. This analysis provides critical insights into the size distribution, stability, and surface charge of the nanocubes, essential for optimizing their synthesis and ensuring consistent quality.

To determine the optimal concentration of green tea extract for nanoparticle synthesis, three different concentrations (50 µg mL⁻¹, 100 µg mL⁻¹, and 150 µg mL⁻¹) were prepared from a stock solution. It was observed that the concentration of 100 µg mL⁻¹ resulted in the formation of the most stable and uniformly sized nanoparticles in cubic shape, indicating this concentration as the optimal condition for biogenic synthesis.

At the initial stage of the reaction (0 hours), the hydrodynamic size of the GS-ZnTPyP-NCs was measured to be 1503.1 ± 12.1 nm (Table S3 and Fig. S6, ESI†). Significant changes in nanocubes size were observed as the reaction progressed. At 12 hours, the size decreased dramatically to 240.6 ± 18 nm, indicating rapid nanoparticle formation and initial stabilization. By 24 hours, the size increased slightly to 339.9 ± 11 nm and remained consistent at 48 hours with the same measurement about 345.7 ± 14 nm (Fig. S6, ESI†).

We employed an HPLC method to analyze the active phytoconstituents and major catechins in green tea extract. The five catechins identified were (+)-catechin (C), (–)-epicatechin (EC), (–)-epicatechin gallate (ECG), (–)-epigallocatechin (EGC), and (–)-epigallocatechin gallate (EGCG) (Fig. S1†). Among these, ECG was found to be the most abundant compound, followed

by EGC and caffeine. Fig. S4c, ESI† presents the chromatogram of the extracted green tea, clearly displaying these compounds, while Table S1† lists their retention times and identifies them based on comparison with reference literature data.²⁷

We hypothesize that the amphiphilic polyphenols present in the green tea extract, such as ECG, EGCG and EGC, facilitate the self-assembly and encapsulation of ZnTPyP monomer within micellar structure. These polyphenols not only facilitate the encapsulation of ZnTPyP but also play a crucial role in stabilizing the nanoparticles. The stabilization occurs through the interaction of enol forms of the phytoconstituents with the nanoparticle surface, preventing aggregation and promoting the growth of nanostructures with the well-defined shape and size. This stabilization mechanism is consistent with previous studies demonstrating the role of plant polyphenols in nanoparticle formation and stabilization.^{28,29} To further strengthen our claim that the green tea extracts-derived ingredients are responsible for the formation of porphyrin nanocubes, we conducted UV-visible and FT-IR spectroscopy for both the green tea extracts and the porphyrin nanocubes. The results revealed the presence of similar functional groups in both the green tea extracts and the GS-ZnTPyP-NCs, thereby providing strong evidence to support our assertion.

The SEM images in Fig. S7, ESI† capture different stages in the self-assembly of GS-ZnTPyP-NCs, providing a visual complement to the DLS data. Fig. S7b, ESI† shows the emergence of large cubical objects approximately 6 hours after the reaction starts. These intermediates are relatively short with round ends, reflecting the early stages of nanoparticle formation observed in the DLS analysis. At approximately 18 h into the reaction, as depicted in Fig. S7c, ESI†, the assembly progresses further, with the coexistence of fully formed nanocubes of ZnTPyP and incomplete structures visible. This intermediate stage corroborates the confined self-assembly and stabilization phases identified through DLS measurements.

The ZnTPyP porphyrin nanoparticles exhibit well-defined morphologies, including nanocubes and nanorods, as depicted in Fig. 1, and possess notable photophysical properties. It was observed that the morphology of ZnTPyP nanoparticles differs significantly between conventional and biogenic synthesis approaches. The conventionally synthesized nanoparticles (CS-ZnTPyP-NPs) exhibited a rod-shaped structure (Fig. 1b). In contrast, the biogenically synthesized nanoparticles (GS-ZnTPyP-NPs) displayed a uniform three-dimensional cube-like morphology (Fig. 1c), with edge lengths of approximately 330.7 nm and a standard deviation of 4.8%. This stark difference in morphology highlights the impact of the synthesis method on the structural characteristics of the nanoparticles. Specifically, the arrangement of porphyrins within the CS-ZnTPyP nanorods and GS-ZnTPyP nanocubes results in significantly broader UV-visible absorption bands that are both red-shifted and enhanced compared to those of the monomeric porphyrin (Fig. 1a).

High-resolution transmission electron microscopy (HR-TEM) (Fig. 1d and S8, ESI†) of GS-ZnTPyP-NCs reveals ordered arrays within a single crystalline wall structure and elemental mapping confirms the presence of zinc metal in it. The HRTEM



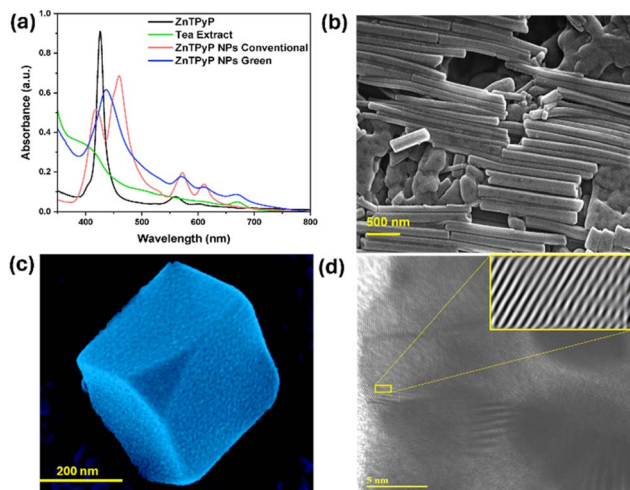


Fig. 1 Characterization data of porphyrinic nanoparticles (a) UV-vis absorption spectra of ZnTPyP, green tea extract, ZnTPyP-NRs synthesized *via* conventional method and ZnTPyP-NCs synthesized *via* bioinspired route. (b) FESEM image of CS-ZnTPyP-NRs. (c) FESEM image of GS-ZnTPyP-NC. (d) HRTEM image of bioinspired GS-ZnTPyP-NCs.

image in Fig. 1d displays a single-crystal lattice fringe with a spacing of 1.7 nm, which is consistent with the π - π stacking configuration of porphyrins.³⁰

Singlet oxygen ($^1\text{O}_2$) induces cytotoxic reactions that result in bacterial cell destruction, and the effectiveness of the antimicrobial sono-photodynamic effect of any sono-photosensitizer is directly related to its singlet oxygen quantum yield (SOQY, Φ_Δ).^{31–33} Consequently, the developed self-assembled porphyrinic nanoparticles were evaluated for their efficiency in generating singlet oxygen (Table S4, ESI†). The generation of singlet oxygen was determined using a 1,3-diphenylisobenzofuran

(DPBF) assay. For this purpose, mixtures of DPBF with the test samples, CS-ZnTPyP-NRs and GS-ZnTPyP-NCs, as well as DPBF alone (blank), were irradiated with ultrasound (1.0 MHz, 1.5 W cm^{-2}) and deep-red light LEDs (670 nm) for 180 seconds. The decrease in the concentration of DPBF, a singlet oxygen chemical quencher, was monitored using UV-vis spectroscopy every 30 seconds, as shown in Fig. 2 and S11, ESI† with the Φ_Δ values listed in Table S4, ESI†. The absorbance intensity showed no significant change within 180 seconds for the group DPBF + US + L (Fig. 2a). In contrast, the GS-ZnTPyP-NCs + DPBF + US + L group exhibited a significant decrease in absorbance intensity, indicating singlet oxygen ($^1\text{O}_2$) generation under combined US and light irradiation (Fig. 2b).

To determine the generation of other reactive oxygen species (ROS) such as hydroxyl radicals ($\cdot\text{OH}$) and superoxide radical anion ($\text{O}_2^{\cdot-}$), similar experiments were performed using methylene blue (MB) and nitroblue tetrazolium (NBT) as probes, respectively (Fig. S11, ESI†). The observed decrease in absorbance for MB and NBT after treatment indicated the production of $\cdot\text{OH}$ and $\text{O}_2^{\cdot-}$, respectively, confirming the ROS generation capability of the ZnTPyP NPs under the experimental conditions. Notably, the CS-ZnTPyP-NRs produced no detectable superoxide radical, whereas the GS-ZnTPyP-NCs generated a high amount of superoxide radical, highlighting a significant difference in their ROS generation profiles (Fig. S11g and h, ESI†).

Continuing from the previous results, a scavenging study was performed to confirm the formation of ROS.³⁴ Specific scavengers were employed for each ROS, with sodium azide (NaN_3) used for $^1\text{O}_2$, isopropanol (IPA) for $\cdot\text{OH}$, and *p*-benzoquinone (*p*-BQ) for $\text{O}_2^{\cdot-}$. ZnTPyP NPs were exposed to combined US and light irradiation (SPDT) in the presence of these scavengers, and the degradation of the respective probes was monitored *via* UV-vis spectroscopy (Fig. S11, ESI†). A significant reduction in probe degradation rates in the presence of the specific scavengers confirmed the successful quenching of the respective ROS, thereby substantiating the formation of $^1\text{O}_2$, $\cdot\text{OH}$, and $\text{O}_2^{\cdot-}$, during SPDT treatment. These findings support and expand upon the earlier evidence of ROS generation by ZnTPyP-NPs.

Further, the results of electron spin resonance (ESR) spectroscopy analysis also confirmed the distinctive $^1\text{O}_2$, $\cdot\text{OH}$ and $\text{O}_2^{\cdot-}$ peaks in an environment containing GS-ZnTPyP-NCs exposed to combined US and light irradiations, and the levels of ROS were much higher than those in the CS-ZnTPyP-NRs group, implying the excellent sono-photocatalytic capability of GS-ZnTPyP-NCs (Fig. S11, ESI†).

The short- and long-term stability of the GS-ZnTPyP-NCs was thoroughly investigated. To assess short-term stability, nanocubes were sampled every 6 hours during preparation and analyzed for particle size, zeta potential, and polydispersity index (PDI) using dynamic light scattering (DLS). The results showed that both mean particle size and zeta potential remained constant over 48 hours, indicating stability under physiological conditions (Fig. S10a, ESI†). Additionally, the low PDI values confirmed a uniform size distribution (Fig. S10b, ESI†). Long-term stability was assessed by storing lyophilized

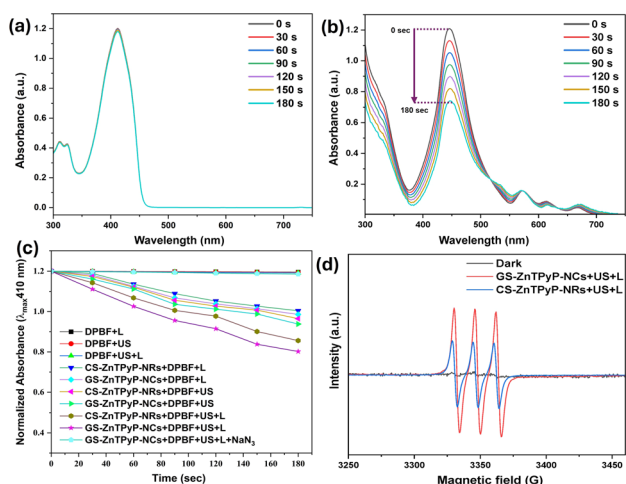


Fig. 2 Determination of the singlet oxygen quantum yield of porphyrinic nanoparticles. Degradation of DPBF as a function of irradiation time under the treatment conditions of (a) DPBF + US + L (b) GS-ZnTPyP-NCs + DPBF + US + L (c) absorbance intensity of DPBF along the irradiation time for different groups. (d) ESR spectra using TEMP as a spin trap agent under different measurement conditions.



nanoparticles at 4 °C for 60 days, with measurements every 15 days. The results showed consistent particle size and zeta potential, confirming long-term stability (Fig. S10c and d, ESI†).

The antibacterial sono-photodynamic (aSPDT) activity of the porphyrinic nanoparticles was assessed against *E. coli* and *S. aureus* using the plate count method (Fig. 3). The number of bacterial colonies significantly decreased in both the GS-ZnTPyP-NCs + US and GS-ZnTPyP-NCs + light groups compared to the control and GS-ZnTPyP-NCs alone. The GS-ZnTPyP-NCs + US + light group demonstrated remarkable antibacterial efficiency, achieving 99.995% against *S. aureus* and 99.92% against *E. coli* with just 20 minutes of combined light and ultrasound treatment.

Moreover, *S. aureus* demonstrated greater susceptibility to aSPDT treatment compared to *E. coli*, aligning with previous research indicating that Gram-positive bacteria are often more responsive to such treatments.³⁵ This differential susceptibility is likely due to the distinct structures of their cell envelopes, which affect their interaction with ROS.

In contrast, while CS-ZnTPyP-NRs also demonstrated antibacterial activity, GS-ZnTPyP-NCs exhibited significantly greater efficacy (Fig. S13, ESI†). Particularly for *S. aureus*, GS-ZnTPyP-NCs achieved nearly complete eradication with only 20 minutes of US + light irradiation at a concentration as low as 50 $\mu\text{g mL}^{-1}$, whereas CS-ZnTPyP-NRs only killed 75% of the bacteria at the same concentration (Fig. S13, ESI†). These results clearly establish GS-ZnTPyP-NCs as a more potent sono-photosensitizer for bacterial eradication compared to CS-ZnTPyP-NRs. This enhanced activity is due to polyphenols present on the surface of the GS-ZnTPyP-NCs, which are derived from the GTE used in their synthesis. These polyphenols act as electron donors, facilitating the reduction of molecular oxygen to superoxide anion ($\text{O}_2^{\cdot-}$). In contrast, CS-ZnTPyP-NRs, synthesized without GTE, lack these polyphenols, resulting in lower superoxide anion production and antibacterial efficacy.

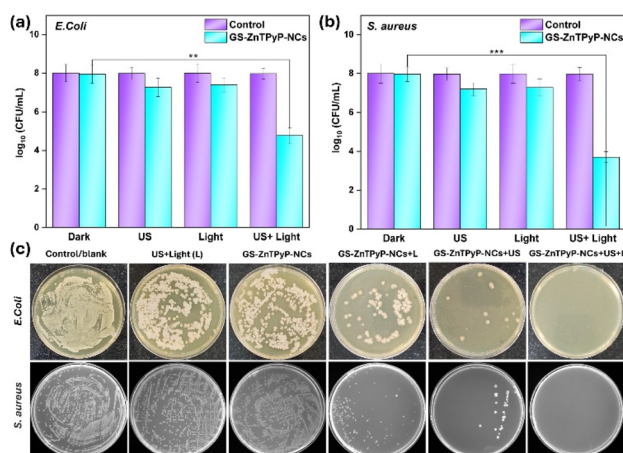


Fig. 3 Antibacterial sono-photodynamic (aSPDT) activity of green ZnTPyP nanocubes (GS-ZnTPyP-NCs). (a and b) The statistical chart of antibacterial effects of (a) *E. coli* and (b) *S. aureus*. (c) Spread plate of *E. coli* and *S. aureus*. Statistical significance between bars (* $p < 0.05$, ** $p < 0.01$, *** $p < 0.001$).

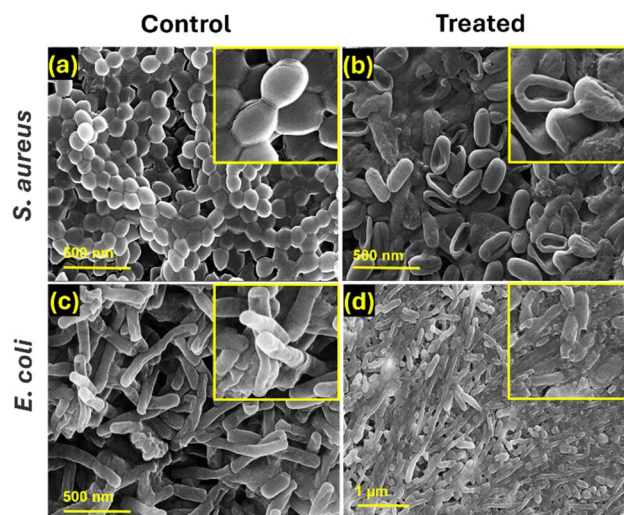


Fig. 4 FESEM micrographs of (a) *S. aureus*, control, inset showing intact cell membrane (b) *S. aureus*, treated with GS-ZnTPyP-NCs + US + L, inset showing damaged cell membrane (c) *E. coli*, control, inset showing intact cell membrane (d) *E. coli* treated with GS-ZnTPyP-NCs + US + L, inset showing damaged cell membrane.

Additionally, green tea extract at a concentration of 0.1 mg mL^{-1} did not show significant antibacterial activity against *S. aureus* and *E. coli* (Fig. S13, ESI†), confirming previous reports that natural extracts possess negligible antibacterial activity.³⁶

Further examination of bacterial morphologies using FESEM images (Fig. 4) confirmed these observations, showing wrinkled, deformed, and broken bacterial membranes in the GS-ZnTPyP-NCs + US + light treated group. In contrast, control group bacteria, both *S. aureus* and *E. coli*, displayed smooth surfaces and intact membranes. Treated bacteria exhibited various degrees of membrane damage, leading to significant bacterial death due to severe membrane disruption and content leakage. These results further demonstrate that GS-ZnTPyP-NCs with dual sono-photo response can achieve excellent antibacterial efficiency at low concentrations in a short time.

Sono-photoinactivation of bacteria using porphyrin combines PDT and SDT mechanisms. PDT generates ROS under light, while SDT uses US-induced acoustic cavitation to enhance ROS production. Sonoluminescence further excite porphyrin, amplifying bacterial inactivation.

Conclusions

In conclusion, the green synthesis of ZnTPyP nanocubes (GS-ZnTPyP-NCs) via tea extract and their application in sono-photodynamic therapy (SPDT) for bacterial inactivation represents a sustainable and effective therapeutic strategy. This eco-friendly approach aligns with green chemistry principles and leverages bioactive compounds for enhanced antibacterial efficacy. The augmented sonodynamic and photodynamic modalities offer a potent solution for combating bacterial infections, highlighting the potential of green nanosynthesis in addressing antibiotic resistance and advancing innovative antimicrobial



therapies. Future research should investigate the *in vivo* efficacy of GS-ZnTPyP-NCs and their use in treating complex infections. Clinically, they could be used for resistant infections, potentially transforming antimicrobial treatments.

Data availability

The data supporting this article have been included as part of the ESI.†

Author contributions

P. S. T.: conceptualization, data curation, investigation, methodology, formal analysis, validation, visualization, and writing – original draft. M. S.: conceptualization, formal analysis, validation, supervision, project administration, writing – review & editing, resources, and funding acquisition.

Conflicts of interest

There are no conflicts to declare.

Acknowledgements

PST gratefully acknowledges the Ministry of Education (MoE), Govt. of India, for providing doctoral fellowship. MS sincerely thank Science and Engineering Research Board (SERB/CRG/2020/005958), New Delhi, for the financial support. Sincere thanks to Institute Instrumentation Centre, Indian Institute of Technology Roorkee, for the various analytical facilities provided.

Notes and references

- 1 A. R. Kirtane, M. Verma, P. Karandikar, J. Furin, R. Langer and G. Traverso, *Nat. Nanotechnol.*, 2021, **16**, 369–384.
- 2 F. Zhou, T. Yu, R. Du, G. Fan, Y. Liu, Z. Liu, J. Xiang, Y. Wang, B. Song, X. Gu, L. Guan, Y. Wei, H. Li, X. Wu, J. Xu, S. Tu, Y. Zhang, H. Chen and B. Cao, *Lancet*, 2020, **395**, 1054–1062.
- 3 S. B. Levy and M. Bonnie, *Nat. Med.*, 2004, **10**, S122–S129.
- 4 E. Bakkeren, M. Diard and W. D. Hardt, *Nat. Rev. Microbiol.*, 2020, **18**, 479–490.
- 5 F. D. Lowy, *N. Engl. J. Med.*, 1998, **339**, 520–532.
- 6 N. A. Turner, B. K. Sharma-Kuinkel, S. A. Maskarinec, E. M. Eichenberger, P. P. Shah, M. Carugati, T. L. Holland and V. G. Fowler, *Nat. Rev. Microbiol.*, 2019, **17**, 203–218.
- 7 B. P. Howden, S. G. Giulieri, T. W. F. Lung, S. L. Baines, L. K. Sharkey, J. Y. H. Lee, A. Hachani, I. R. Monk and T. P. Stinear, *Nat. Rev. Microbiol.*, 2023, **21**, 380–395.
- 8 N. S. Thakur, J. Bhaumik, S. Kirar and U. C. Banerjee, *ACS Sustain. Chem. Eng.*, 2017, **5**, 7950–7960.
- 9 D. S. Chormey, B. T. Zaman, T. B. Kustanto, S. E. Bodur, S. Bodur, Z. Tekin, O. Nejati and S. Bakırdere, *Nanoscale*, 2023, **15**, 19423–19447.
- 10 M. N. Nadagouda and R. S. Varma, *Green Chem.*, 2006, **8**, 516–518.
- 11 M. N. Nadagouda and R. S. Varma, *Green Chem.*, 2008, **10**, 859–886.
- 12 S. Asefian and M. Ghavam, *BMC Biotechnol.*, 2024, **24**, 1–22.
- 13 C. Xu, S. Zhou, H. Song, H. Hu, Y. Yang, X. Zhang, S. Ma, X. Feng, Y. Pan, S. Gong, F. Fan, P. Chen and Q. Chu, *Nano Today*, 2023, **52**, 101990.
- 14 A. Wirwis and Z. Sadowski, *ACS Omega*, 2023, **8**, 30532–30549.
- 15 P. Plachtová, Z. Medříková, R. Zbořil, J. Tuček, R. S. Varma and B. Maršálek, *ACS Sustain. Chem. Eng.*, 2018, **6**, 8679–8687.
- 16 H. Hu, J. Zhao, K. Ma, J. Wang, X. Wang, T. Mao, C. Xiang, H. Luo, Y. Cheng, M. Yu, Y. Qin, K. Yang, Q. Li, Y. Sun and S. Wang, *J. Controlled Release*, 2023, **359**, 188–205.
- 17 Q. Yu, C. Wang, X. Zhang, H. Chen, M. X. Wu and M. Lu, *ACS Nano*, 2024, **18**, 14085–14122.
- 18 R. Zhang, D. Yang, P. Zang, F. He, S. Gai, Y. Kuang, G. Yang, P. Yang, R. Zhang, D. Yang, P. Zang, F. He, S. Gai, P. Yang, Y. Kuang and G. Yang, *Adv. Mater.*, 2023, 2308355.
- 19 S. Guo, G. Shu, H. Luo, X. Kuang, L. Zheng, C. Wang, C.-A. Zhou, L. Song, K. Ma and H. Yue, *ACS Appl. Mater. Interfaces*, 2024, **16**, 24410–24420.
- 20 Z. Weng, Q. Wei, C. Ye, Y. Xu, J. Gao, W. Zhang, L. Liu, Y. Zhang, J. Hu, Q. Zhong, J. Sun and X. Wang, *ACS Nano*, 2024, **18**, 5180–5195.
- 21 Z. Li, Z. Zhang, L. Ma, H. Wen, M. Kang, D. Li, W. Zhang, S. Luo, W. Wang, M. Zhang, D. Wang, H. Li, X. Li and H. Wang, *Angew. Chem., Int. Ed.*, 2024, **63**, e202400049.
- 22 C. He, P. Feng, M. Hao, Y. Tang, X. Wu, W. Cui, J. Ma and C. Ke, *Adv. Funct. Mater.*, 2024, 2402588.
- 23 P. Geng, Y. Li, D. K. Macharia, X. Ren, R. Meng, W. Wang, H. Lan and S. Xiao, *J. Colloid Interface Sci.*, 2024, **660**, 1021–1029.
- 24 P. Xu, C. Wen, C. Gao, H. Liu, Y. Li, X. Guo, X. C. Shen and H. Liang, *ACS Nano*, 2024, **18**, 713–727.
- 25 P. S. Thakur, L. Gautam, S. P. Vyas and M. Sankar, in *Inorganic Nanosystems*, Elsevier, 2023, pp. 489–507.
- 26 J. Chen, Q. Zhou and W. Cao, *Adv. Funct. Mater.*, 2024, 2405844.
- 27 P. L. Fernández, M. J. Martín, A. G. González and F. Pablos, *Analyst*, 2000, **125**, 421–425.
- 28 J. E. Chung, S. Tan, S. J. Gao, N. Yongvongsoontorn, S. H. Kim, J. H. Lee, H. S. Choi, H. Yano, L. Zhuo, M. Kurisawa and J. Y. Ying, *Nat. Nanotechnol.*, 2014, **9**, 907–912.
- 29 S. Xiong, S. Tan, P. Huang, Y. Li, J. E. Chung, M. Kurisawa, D. Zink and J. Y. Ying, *Biomater. Sci.*, 2023, **11**, 4675–4683.
- 30 J. Wang, Y. Zhong, L. Wang, N. Zhang, R. Cao, K. Bian, L. Alarid, R. E. Haddad, F. Bai and H. Fan, *Nano Lett.*, 2016, **16**, 6523–6528.
- 31 D. Sun, Z. Zhang, M. Chen, Y. Zhang, J. Amagat, S. Kang, Y. Zheng, B. Hu and M. Chen, *ACS Appl. Mater. Interfaces*, 2020, **12**, 40728–40739.
- 32 E. Güzel, G. Y. Atmaca, A. E. Kuznetsov, A. Turkkol, M. D. Bilgin and A. Erdoğan, *ACS Appl. Bio Mater.*, 2022, **5**, 1139–1150.



- 33 A. Turkkol, C. C. Karanlık, S. G. Caliskan, M. D. Bilgin, A. Erdoğan and E. Güzel, *ACS Appl. Bio Mater.*, 2024, **7**, 2725–2733.
- 34 A. Selim, S. Kaur, A. H. Dar, S. Sartaliya and G. Jayamurugan, *ACS Omega*, 2020, **5**, 22603–22613.
- 35 H. Liu, J. Li, X. Liu, Z. Li, Y. Zhang, Y. Liang, Y. Zheng, S. Zhu, Z. Cui and S. Wu, *ACS Nano*, 2021, **15**, 18505–18519.
- 36 J. Gopal, M. Muthu, D. Paul, D. H. Kim and S. Chun, *Sci. Rep.*, 2016, **6**, 1–14.

